Princeton Plasma Physics Laboratory

PPPL-

PPPL-

Princeton Plasma Physics Laboratory
Report Disclaimers

Full Legal Disclaimer

Trademark Disclaimer

PPPL Report Availability

Princeton Plasma Physics Laboratory:

http://www.pppl.gov/techreports.cfm

Office of Scientific and Technical Information (OSTI):

http://www.osti.gov/bridge

Related Links:

U.S. Department of Energy

Office of Scientific and Technical Information

Fusion Links

Numerical calculation of neoclassical distribution functions and current profiles in low collisionality, axisymmetric plasmas

B.C. Lyons,[1] S.C. Jardin,[2] and J.J. Ramos[3]

[1] *Program in Plasma Physics, Princeton University, Princeton, New Jersey 08543-0451, USA*

[2] *Princeton Plasma Physics Laboratory, Princeton, New Jersey 08543-0451, USA*

[3] *Plasma Science and Fusion Center, Massachusetts Institute of Technology, Cambridge, Massachusetts 02139-4307, USA*

A new code, the Neoclassical Ion-Electron Solver (NIES), has been written to solve for stationary, axisymmetric distribution functions (f) in the conventional banana regime for both ions and electrons using a set of drift-kinetic equations (DKEs) with linearized Fokker-Planck-Landau collision operators. Solvability conditions on the DKEs determine the relevant non-adiabatic pieces of f (called h). We work in a 4D phase space in which ψ defines a flux surface, θ is the poloidal angle, v is the total velocity referenced to the mean flow velocity, and λ is the dimensionless magnetic moment parameter. We expand h in finite elements in both v and λ. The Rosenbluth potentials, Φ and Ψ, which define the integral part of the collision operator, are expanded in Legendre series in $\cos\chi$, where χ is the pitch angle, Fourier series in $\cos\theta$, and finite elements in v. At each ψ, we solve a block tridiagonal system for h_i (independent of f_e), then solve another block tridiagonal system for h_e (dependent on f_i). We demonstrate that such a formulation can be accurately and efficiently solved. NIES is coupled to the MHD equilibrium code JSOLVER [J. DeLucia, *et al.*, J. Comput. Phys. **37**, pp 183-204 (1980).] allowing us to work with realistic magnetic geometries. The bootstrap current is calculated as a simple moment of the distribution function. Results are benchmarked against the Sauter analytic formulas and can be used as a kinetic closure for an MHD code (e.g., M3D-C1 [S.C. Jardin, *et al.*, Computational Science & Discovery, **4** (2012).]).

I. INTRODUCTION

There are numerous causes for the sudden and catastrophic loss of toroidal plasma confinement. These disruptions can be set off, for example, by a piece of debris entering the plasma, a buildup of high-Z impurities leading to radiative collapse, or the crossing of magnetohydrodynamics (MHD) stability thresholds. One of the most common causes of disruptions is the neoclassical tearing mode (NTM). NTMs can occur when the temperature and pressure profiles flatten across a magnetic island in the core of a toroidally-confined plasma. This causes a reduction in the neoclassical bootstrap current, driven by gradients in these profiles, within the island. As the bootstrap current outside of the island remains unaffected, the resulting hole in the bootstrap current profile can lead to further growth in the island size. If the island grows large enough such that it alters the macroscopic magnetic equilibrium, the plasma can become MHD unstable and confinement is lost. A recent study on the Joint European Torus[1] (JET) found that these NTMs are the single most common root cause of disruptions[2]. Avoidance of these modes is expected to place a severe limit on plasma β for the ITER[3] experiment, in which very few disruptions can be tolerated[4]. Thus, a good understanding of and predictive capability for NTMs is crucial to the success of the ITER campaign.

A realistic and accurate numerical study of neoclassical tearing modes, in addition to several other core plasma instabilities, such as sawtooth modes, requires a hybrid code. Such simulations must accurately account for both the kinetic trapped particle dynamics that produce the bootstrap current and the magnetohydrodynamic evolution of the plasma equilibrium due to changes in the current profile. Furthermore, as magnetic islands are inherently three-dimensional structures, the code must work for nonaxisymmetric magnetic geometries. While sophisticated, three-dimensional MHD time evolution codes exist (e.g., NIMROD[5] and M3D-C1[6]), it is more difficult to find kinetic neoclassical codes that can be used in such a study. The XGC0[7] and DKES[8] codes do solve for the bootstrap current in 3D toroidal geometries. XGC0, however, is a PIC code that requires enormous computing power. DKES uses a variational method to calculate neoclassical quantities but uses the Lorentz collision operator, which includes only pitch angle scattering. While this is the dominant process for electron-ion collisions in low-collisionality plasmas (such as those found in the cores of reactor-grade, toroidally-confined plasmas that we would like to study), energy scattering is just as important for like-particle collisions[9]. As Belli and Candy recently showed[10], the use of model collision operators to study the bootstrap current, even ones substantially

more sophisticated than the Lorentz operator, can lead to errors of 5-10% compared to the full Fokker-Planck-Landau collision operator. Furthermore, the DKES code has been found to have difficulty converging at extremely low collsionalities[11]. Several other neoclassical codes are widely used in the community, including NCLASS[12], CQLP/CQL3D[13,14], and NEO[10,15]. The NCLASS code uses a truncated form of the Hirshman-Sigmar[16] moment expansion of the collision operator and evaluates just the corresponding lower moments of the distribution functions. The CQLP/CQL3D codes include the complete nonlinear Fokker-Planck-Landau collision operator, while the most recent version of the NEO code[10] uses the complete linearized Fokker-Planck-Landau collision operator. Both then solve for the full distribution functions. All of these codes, however, assume a 2D axisymmetric toroidal geometry, limiting their use in studies involving magnetic islands. Thus, we require a new code that is applicable to the cores of high-temperature fusion plasmas and has the ability to study neoclassical dynamics in three spatial dimensions.

An appropriate analytic model that could form the basis of such a code has been developed in Refs. [9, 17]. It features a coupled system of ion and electron fluid and drift-kinetic (DKE) equations in general 3D real space and 2D (gyroaveraged) velocity space with Fokker-Planck-Landau linearized collision operators. The equations follow an asymptotic expansion in the small parameter $\delta \sim \rho_i/L \ll 1$, the ratio of the ion gyroradius to the macroscopic scale lengths. Additional orderings of small mass ratio between electrons and ions and of low collisionality relevant to the high temperature plasmas of fusion interest are assumed, such that

$$(m_e/m_i)^{1/2} \sim \nu_* \sim \delta. \quad (1)$$

Here, the dimensionless collisionality parameter $\nu_* \sim L/\lambda^{coll}$ is the ratio between the macroscopic length scale and the collisional mean free path (for all species with comparable temperatures) $\lambda^{coll} = v_{ths}/\nu_s$, with v_{ths} and ν_s as the thermal velocity and the collision frequency of species s. This mass ratio ordering results in the ratio of the electron gyroradius to the macroscopic scale being $\delta_e \sim \rho_e/L \sim \delta^2$. The expansion is carried consistently to the frequency scale where collisions begin to influence the dynamics, $\omega^{coll} \sim \delta^2 v_{thi}/L \sim \delta^3 v_{the}/L$. Thus the electron DKE contains terms of order $\delta^3 \sim \delta_e \nu_*$ but not $\delta^4 \sim \delta_e^2$. This is the conventional neoclassical ordering in the banana regime. For the ions, however, second-order terms in the ion gyroradius parameter δ are kept, accounting for finite banana-width effects.

A numerical solution of this complete set of equa-

tions would provide a closure for an extended MHD code, ideally suited for studying macroscopic core plasma phenomena like NTMs. The equations are complex, however, and there is no guarantee that an efficient computational method could be found that would make such hybrid fluid and drift-kinetic simulations feasible. Thus, it is prudent to first examine these equations in some reduced form. In this paper, we present a new code, the Neoclassical Ion-Electron Solver (NIES) that solves the ion and electron stationary DKEs in an axisymmetric geometry, considering the leading low-collisionality contributions under the conventional neoclassical banana ordering for both species. This means relaxing the conditions of Eq. 1 to

$$(m_e/m_i)^{1/2} \sim \delta, \quad 1 \gg \nu_* \gg \delta, \quad (2)$$

so that the ion DKE needs to retain only its first-order in δ terms and a direct comparison with conventional neoclassical banana results can be carried out. In Section II, we present the spatially two-dimensional axisymmetric equations to be solved (in CGS units), expressed in the mean flow reference frame representation as derived in Ref. [9]. We then describe in Section III the expansions and computational methods that have been used in NIES. Results from the code are discussed in Section IV, including convergence studies and a benchmark of the Sauter analytic fits[18] for the neoclassical equilibrium flows and bootstrap current.

II. ANALYTIC MODEL

In a time-independent, axisymmetric toroidal system, the electromagnetic fields can be written as

$$\mathbf{B} = \nabla\psi \times \nabla\zeta + RB_\zeta \nabla\zeta \quad (3)$$

$$\mathbf{E} = -\nabla V - V_0 \nabla\zeta. \quad (4)$$

Here, ψ is the poloidal flux per radian (a constant on each nested flux surface), ζ is the azimuthal angle, V is the single-valued electric potential and $2\pi V_0$ is the constant toroidal loop voltage. We take the plasma to be quasineutral and to contain a single ion species, and we assume, for simplicity, the ion charge to be $Z = 1$ ($e_i = -e_e = e$, $n_i = n_e = n$).

In their leading order, the density, temperatures, electric potential and RB_ζ are flux functions: $n(\psi)$, $T_s(\psi)$, $V(\psi)$, and $I(\psi) \equiv RB_\zeta$. In addition, the leading-order mean flow velocity of each species is

$$\mathbf{u}_s = U_s(\psi)\mathbf{B} + cR^2 \left[\frac{dV}{d\psi} + \frac{1}{e_s n} \frac{d(nT_s)}{d\psi} \right] \nabla\zeta, \quad (5)$$

where U_s is the parallel flow stream function of species s, such that $dI/d\psi = en(U_i - U_e)$.

As has been shown in past work[9], retaining first-order accuracy in its Larmor radius, $\delta_s = \rho_s/L$, and referred to the moving frame of its mean flow, the gyroaveraged distribution function of species s can be expressed as

$$\bar{f}_s = \left(1 + g_{s,0} + g_{s,1}\ v_\parallel\right) f_{Ms} + h_s. \qquad (6)$$

Here, f_{Ms} is the leading-order Maxwellian defined as

$$f_{Ms} = \frac{n}{(2\pi)^{3/2} v_{ths}^3} \exp\left(-\frac{v^2}{2v_{ths}^2}\right) \qquad (7)$$

with $v_{ths} = \sqrt{T_s/m_s}$,

$$g_{s,0} = -\frac{e_s \Delta V}{T_s} - \frac{\Delta n}{n} - \left(\frac{m_s v^2}{T_s} - 3\right)\frac{\Delta T_s}{2T_s} \qquad (8)$$

represents a perturbative redefinition of the Maxwellian with ΔV, Δn and ΔT_s equal to the differences between the actual electric potential, density and temperatures and their leading-order $V(\psi)$, $n(\psi)$ and $T_s(\psi)$, and

$$g_{s,1} = -\left[\frac{m_s U_s B}{T_s} - \frac{m_s c I}{2e_s B T_s}\left(\frac{m_s v^2}{T_s} - 5\right)\frac{dT_s}{d\psi}\right]. \qquad (9)$$

The last term, h_s, is the so-called non-adiabatic piece which obeys the reduced drift-kinetic equation

$$v_\parallel (\mathbf{b} \cdot \nabla\theta)\frac{\partial h_s}{\partial \theta} - C_s[h_s] = S_s v_\parallel. \qquad (10)$$

We work in the four-dimensional phase space defined by $(\psi, \theta, v, \lambda)$ where θ is the poloidal angle and v is the magnitude of the random velocity in the moving frame of the considered species' mean flow. The dimensionless magnetic moment parameter λ is defined by

$$\lambda(\psi, \theta, \chi) = \sin^2\chi\frac{B_{max}(\psi)}{B(\psi, \theta)}, \qquad (11)$$

where $\chi = \arctan(v_\perp/v_\parallel)$ is the pitch angle and $B_{max}(\psi)$ is the maximum value of B on the ψ flux surface. We note that λ is an adiabatic invariant; particles with $\lambda < 1$ are passing particles, while those with $\lambda > 1$ are trapped particles. In terms of the phase space variables $(\psi, \theta, v, \lambda)$, the moving frame relative parallel velocity is the double-valued function

$$v_\parallel(\psi, \theta, v, \lambda) = \pm v\left[1 - \lambda B(\psi, \theta)/B_{max}(\psi)\right]^{1/2}. \qquad (12)$$

Consistent with our mean flow reference frame representation, the function $g_{s,1}$ (9) has the non-standard term proportional to U_s and the non-Maxwellian part of the distribution function, $\bar{f}_s - f_{Ms}$, is such that its $v_\parallel$ moment vanishes.

The collision operator C_s in Eq. 10 is the gyroaverage of the homogeneous component of the linearized Fokker-Planck-Landau operator. In general, we maintain the operator to the order of $C_s[h_s] \sim \nu_s \delta_s f_{Ms}$, though, for electrons, we also keep several terms of higher order in order to ensure the regularity of the equation near $v = 0$. Here we have introduced the collision frequency of species s, defined by

$$\nu_s = \frac{4\pi e^4 n \ln\Lambda_s}{m_s^2 v_{ths}^3}. \qquad (13)$$

Thus, our form of the collision operator is

$$C_s[h_s] = \nu_{Ds}(\psi, v)\mathcal{L}[h_s] + \frac{\nu_s v_{ths}^3}{v^2}\frac{\partial}{\partial v}\left\{\xi_s\left[v\frac{\partial h_s}{\partial v} + \frac{v^2}{v_{ths}^2}h_s\right] + \xi_{s'}\left[v\frac{\partial h_s}{\partial v} + \frac{m_s v^2}{m_{s'} v_{ths'}^2}h_s\right]\right\}$$
$$+ \frac{\nu_s v_{ths}}{n}f_{Ms}\left(4\pi v_{ths}^2 h_s - \Phi_s[h_s] + \frac{v^2}{v_{ths}^2}\frac{\partial^2 \Psi_s[h_s]}{\partial v^2}\right). \qquad (14)$$

Here,

$$\nu_{Ds}(\psi, v) = \frac{\nu_s v_{ths}^3}{v^3}\left[\varphi_s - \xi_s + \varphi_{s'} - \xi_{s'}\right], \qquad (15)$$

where φ_s is the error function and ξ_s is the Chan-

drasekhar function, each of argument v/v_{ths}:

$$\varphi_s = \varphi\left(x = \frac{v}{v_{ths}}\right) = \frac{2}{\sqrt{2\pi}}\int_0^x \exp(-t^2/2)dt \qquad (16)$$

$$\xi_s = \xi \left(x = \frac{v}{v_{ths}} \right) = \frac{1}{x^2} \left[\varphi(x) - \frac{2x}{\sqrt{2\pi}} \exp(-x^2/2) \right];$$

$$\tag{17}$$

the Lorentz operator is

$$\mathcal{L}[h_s] = \frac{2B_{max}v_\parallel}{Bv^2} \frac{\partial}{\partial \lambda} \left(\lambda v_\parallel \frac{\partial h_s}{\partial \lambda} \right) \tag{18}$$

and the variables $\Phi_s[h_s]$ and $\Psi_s[h_s]$ are the Rosenbluth potentials, defined by

$$\frac{1}{v^2} \frac{d}{dv} \left(v^2 \frac{\partial \Phi_s}{\partial v} \right) + \frac{1}{v^2 \sin \chi} \frac{\partial}{\partial \chi} \left(\sin \chi \frac{\partial \Phi_s}{\partial \chi} \right) = -4\pi h_s \tag{19}$$

$$\frac{1}{v^2} \frac{d}{dv} \left(v^2 \frac{\partial \Psi_s}{\partial v} \right) + \frac{1}{v^2 \sin \chi} \frac{\partial}{\partial \chi} \left(\sin \chi \frac{\partial \Psi_s}{\partial \chi} \right) = \Phi_s. \tag{20}$$

We have chosen to express the equations for the Rosenbluth potentials (i.e. the integral part of the collision operator) in the (v, χ) variables, while the rest of the collision operator (i.e. its differential part) remains expressed in the (v, λ) variables. This will prove advantageous for the algorithm that will be used in our numerical solution of the drift-kinetic equation. In Eqs. 14 and 15, the terms containing s' are due to collisional cross-species interactions. They are present for the electrons ($s = e$) as they interact with both themselves and the ions ($s' = i$). The ions ($s = i$), however, only interact appreciably with themselves due to their large relative mass. Thus, the terms that would indicate interaction with electrons ($s' = e$) are taken to be zero in the ion case.

The right-hand side of Eq. 10 represents the source terms that drive the neoclassical distribution function. For electrons, it can be shown[9] that

$$S_e = \left\{ \frac{eV_0 I}{T_e BR^2} + \nu_e \left(U_i B + \frac{cI}{enB} \frac{dP}{d\psi} \right) \frac{v_{the}}{v_{thi}^2 v} \xi_i \right.$$
$$+ \frac{\nu_e m_e cI}{eBT_e} \frac{dT_e}{d\psi} \frac{v_{the}}{v} \left[2\varphi_e - 10\xi_e \right.$$
$$\left. \left. + \frac{1}{2}\varphi_i - \frac{5v_{the}^2}{2v_{thi}^2}\xi_i \right] \right\} f_{Me}, \tag{21}$$

where $P = n(T_i + T_e)$ is the total pressure. Each term represents, in order, the ohmic drive, interaction with the ion flow due to collisional friction, pressure gradient drive, and electron temperature gradient drive. For the ions, we again drop terms that would involve interaction with the electrons in addition to the ohmic drive term, because of the large relative ion mass. Thus, the source for the ions is only the ion temperature gradient drive, given by

$$S_i = -\frac{\nu_i m_i cI}{eBT_i} \frac{dT_i}{d\psi} \frac{v_{thi}}{v} \left[2\varphi_i - 10\xi_i \right] f_{Mi}. \tag{22}$$

Since Eq. 10 has the same form as the standard neoclassical drift-kinetic equation[16,19,20], its perturbative solution in the conventional banana regime characterized by $\delta_s \ll \nu_{*s} \ll 1$ is

$$h_s = \varsigma(v_\parallel) H(1 - \lambda) K_s(\psi, v, \lambda) + h_s^{even}(\psi, \theta, v, \lambda). \tag{23}$$

Here, $\varsigma(v_\parallel) = \text{sign}(v_\parallel) = \pm 1$ and H is the Heavyside step function. Whereas the first term in Eq. 23, ςHK_s, is odd with respect to $v_\parallel$, includes only passing particles and is ordered as $O(\delta_s f_{Ms})$, h_s^{even} is even with respect to $v_\parallel$, includes both passing and trapped particles and is of the order of $\delta_s \nu_{*s} f_{Ms}$. This higher-order term obeys the equation

$$v_\parallel (\mathbf{b} \cdot \nabla \theta) \frac{\partial h_s^{even}}{\partial \theta} - C_s \left[\varsigma HK_s \right] = S_s v_\parallel. \tag{24}$$

Dividing by $v_\parallel$ and taking the contour integral of Eq. 24 along a magnetic field line at constant ψ, v, and λ yields

$$\oint_{\psi,v,\lambda} \frac{dl}{v_\parallel} C_s \left[\varsigma HK_s \right] = -\oint_{\psi,v,\lambda} dl S_s, \tag{25}$$

where the contour is taken between the turning points for trapped particles and over one complete poloidal turn for passing particles. For simplicity, we rewrite Eq. 25 in symbolic shorthand form as

$$\mathcal{C}_s[K_s] = -\mathcal{S}_s. \tag{26}$$

The above solvability condition is satisfied trivially for $\lambda > 1$ (i.e., the trapped particles). In the passing domain with $\lambda < 1$, Eq. 25 must be solved numerically to determine the form of K_s. Having done so, the condition that $\bar{f}_s - f_{Ms}$ has zero parallel velocity moment determines the parallel flow stream function as

$$U_s(\psi) = \frac{2\pi}{nB_{max}} \int_0^\infty dv v^3 \int_0^1 d\lambda K_s(\psi, v, \lambda). \tag{27}$$

Since, from Eq. 5, the parallel current is

$$j_\parallel = en\mathbf{b} \cdot (\mathbf{u}_i - \mathbf{u}_e) = en(U_i - U_e)B + \frac{cI}{B}\frac{dP}{d\psi}, \tag{28}$$

knowledge of K_i and K_e allows us to calculate the leading-order ohmic and bootstrap currents for small collisionality and gyroradii.

III. COMPUTATIONAL METHODS

A. Fundamental Equations

Eqs. 19, 20, and 26 form a set of coupled integral-differential equations that define K_s, Φ_s, and Ψ_s.

While, for a given magnetic field, the ion equations are completely closed, the electron source term, Eq. 21, requires knowledge of the ion solution, K_i, in order to determine U_i. Thus, we need to solve Eqs. 26 and 27 for the ions first; then we can use this solution to solve for K_e completely. Furthermore, the set of equations contains no integrals or derivatives with respect to ψ. This allows us to solve for U_i and U_e on one flux surface at a time and to treat ψ as just a parameter in the equations. Accordingly, from now on we shall drop ψ when writing the arguments of functions. We note that solving for U_i and U_e involves generally the same algorithm and that in the following discussion, we treat U_i as some known quantity when solving the electron equations.

As we must solve Eq. 26 in the passing domain,

the contour integral is taken to be

$$\oint_{\psi,v,\lambda} dl \cdots = \int_0^{2\pi} d\theta B \mathcal{J} \cdots , \qquad (29)$$

where $\mathcal{J} = [\nabla\psi \times \nabla\theta \cdot \nabla\zeta]^{-1}$ is the Jacobian defined by the magnetic equilibrium. Then, applying the contour integral to Eq. 14 (divided by $v_\parallel$) and calling

$$y(\theta,\lambda) = \cos\chi = \left[1 - \lambda\frac{B}{B_{max}}\right]^{1/2}, \qquad (30)$$

the left-hand side of Eq. 26 becomes

$$
\begin{aligned}
\mathcal{C}_s[K_s] = {} & \frac{2\nu_{Ds}(v)}{v}\frac{\partial}{\partial\lambda}\left(\eta_1(\lambda)\lambda\frac{\partial K_s}{\partial\lambda}\right) - \frac{\nu_s v_{ths}}{nv}f_{Ms}\int_0^{2\pi}\frac{\mathcal{J}B}{y(\theta,\lambda)}\Phi_s d\theta + \frac{\nu_s v}{nv_{ths}}f_{Ms}\frac{d^2}{dv^2}\int_0^{2\pi}\frac{\mathcal{J}B}{y(\theta,\lambda)}\Psi_s d\theta \\
& + \nu_s\eta_2(\lambda)\frac{v_{ths}^3}{v^3}\left[\frac{\partial}{\partial v}\left\{\xi_s\left[v\frac{\partial K_s}{\partial v} + \frac{v^2}{v_{ths}^2}K_s\right] + \xi_{s'}\left[v\frac{\partial K_s}{\partial v} + \frac{m_s v^2}{m_{s'}v_{ths'}^2}K_s\right]\right\} + \frac{4\pi}{n}v^2 f_{Ms}K_s\right]. \quad (31)
\end{aligned}
$$

Here we have made use of the fact that the integrals are taken with ψ, v, and λ held constant and that K_s does not depend on θ. We have defined two functions entirely determined by the magnetic equilibrium:

$$\eta_1(\lambda) = B_{max}\int_0^{2\pi}\mathcal{J}y(\theta,\lambda)d\theta \qquad (32)$$

$$\eta_2(\lambda) = \int_0^{2\pi}\frac{\mathcal{J}B}{y(\theta,\lambda)}d\theta. \qquad (33)$$

Next, we expand the Rosenbluth potentials in a Legendre series in $\cos\chi$ and Fourier series in $\cos\theta$ (for an equilibrium with up-down symmetry):

$$\begin{pmatrix}\Phi_s \\ \Psi_s\end{pmatrix} = \sum_{m=0}^{M}\sum_{l=1,odd}^{2L-1}\begin{pmatrix}\Phi_s^{l,m}(v) \\ \Psi_s^{l,m}(v)\end{pmatrix}P_l(y)\cos m\theta, \tag{34}$$

where only the odd l's are kept because the source of the Poisson equations for Φ_s and Ψ_s is odd in $v_\parallel$. The integers M and L are determined by how many modes in each series are needed to reach convergence of the solution.

Defining

$$a^{l,m}(\lambda) = \int_0^{2\pi}\frac{\mathcal{J}B}{y(\theta,\lambda)}P_l(y)\cos m\theta d\theta, \qquad (35)$$

we can rewrite Eq. 31 as

$$
\begin{aligned}
\mathcal{C}_s[K_s] = {} & \frac{2\nu_{Ds}(v)}{v}\frac{\partial}{\partial\lambda}\left(\eta_1(\lambda)\lambda\frac{\partial K_s}{\partial\lambda}\right) - \frac{\nu_s v_{ths}}{nv}f_{Ms}a^{l,m}\Phi_s^{l,m} + \frac{\nu_s v}{nv_{ths}}f_{Ms}a^{l,m}\frac{d^2}{dv^2}\Psi_s^{l,m} \\
& + \nu_s\eta_2(\lambda)\frac{v_{ths}^3}{v^3}\left[\frac{\partial}{\partial v}\left\{\xi_s\left[v\frac{\partial K_s}{\partial v} + \frac{v^2}{v_{ths}^2}K_s\right] + \xi_{s'}\left[v\frac{\partial K_s}{\partial v} + \frac{m_s v^2}{m_{s'}v_{ths'}^2}K_s\right]\right\} + \frac{4\pi}{n}v^2 f_{Ms}K_s\right] \quad (36)
\end{aligned}
$$

where the sum over the repeated indices l and m is implied. This, by Eq. 26 must equal $-\mathcal{S}_s$. Applying

the integral along the field line to Eq. 21, we find that

$$\mathcal{S}_e = \left\{ \frac{eV_0 I}{T_e} \int_0^{2\pi} \frac{\mathcal{J}}{R^2} d\theta \right.$$
$$+ \frac{\nu_e v_{the}}{v_{thi}^2 v} \xi_i \left(U_i \int_0^{2\pi} \mathcal{J} B^2 d\theta + \frac{cI}{en} \frac{dP}{d\psi} \int_0^{2\pi} \mathcal{J} d\theta \right)$$
$$+ \frac{\nu_e m_e cI}{eT_e} \frac{dT_e}{d\psi} \frac{v_{the}}{v} [2\varphi_e - 10\xi_e$$
$$\left. + \frac{1}{2}\varphi_i - \frac{5v_{the}^2}{2v_{thi}^2}\xi_i \right] \int_0^{2\pi} \mathcal{J} d\theta \right\} f_{Me} \qquad (37)$$

and, from Eq. 22,

$$\mathcal{S}_i = -\frac{\nu_i m_i cI}{eT_i} \frac{dT_i}{d\psi} \frac{v_{thi}}{v} [2\varphi_i - 10\xi_i] f_{Mi} \int_0^{2\pi} \mathcal{J} d\theta. \qquad (38)$$

Next, we must determine $\Phi_s^{l,m}$ and $\Psi_s^{l,m}$. Plugging

Eq. 34 into Eqs. 19 and 20, then using the identities

$$\frac{1}{\sin\chi} \frac{\partial}{\partial\chi} \left[\sin\chi \frac{\partial}{\partial\chi} P_l(y) \right] = -l(l+1)P_l(y), \quad (39)$$

$$\int_0^\pi P_l(y)P_{l'}(y)\sin\chi d\chi = \frac{2}{2l+1}\delta_{ll'}, \qquad (40)$$

and

$$\int_0^{2\pi} \cos m\theta \cos m'\theta d\theta = \pi\delta_{mm'}(1+\delta_{m0}), \qquad (41)$$

we find a set of equations for each (l,m) that are independent of each other:

$$\frac{1}{v^2}\frac{d}{dv}\left(v^2\frac{\partial\Phi_s^{l,m}}{\partial v}\right) - \frac{l(l+1)}{v^2}\Phi_s^{l,m} = b_s^{l,m} \qquad (42)$$

$$\frac{1}{v^2}\frac{d}{dv}\left(v^2\frac{\partial\Psi_s^{l,m}}{\partial v}\right) - \frac{l(l+1)}{v^2}\Psi_s^{l,m} = \Phi_s^{l,m}. \qquad (43)$$

The inhomogeneous term $b_s^{l,m}$ results from the inner product of $P_l(\cos\chi)$ and $\cos m\theta$ with the source $-4\pi\varsigma HK_s$:

$$b_s^{l,m}(v) = -\frac{2(2l+1)}{1+\delta_{m,0}} \int_0^{2\pi} \cos m\theta \int_0^1 P_l(y) K_s(v,\lambda) \frac{B}{yB_{max}} d\lambda d\theta. \qquad (44)$$

B. Boundary conditions

The boundary conditions to be imposed on $K_s(v,\lambda)$ are:

$$K_s(v=0,\lambda) = 0 \qquad (45)$$

$$K_s(v=v_{max},\lambda) = 0 \qquad (46)$$

$$lim_{\lambda\to 0} \lambda^{1/2}\frac{\partial K_s(v,\lambda)}{\partial\lambda} = 0 \qquad (47)$$

$$K_s(v,\lambda=1) = 0. \qquad (48)$$

Eq. 45 is required so that ςHK_s is continuous and vanishes at $v=0$ since it is odd in $v_\parallel$. Eq. 46 is truly a condition at $v=\infty$ and ensures the physical condition that the distribution function decays at large velocities. Since the driving terms in Eqs. 21 and 22 are all proportional to f_{Ms}, the solution should drop

rapidly to zero beyond a few multiples of v_{ths}. Thus, it will be sufficient to take $K_s(v=v_{max},\lambda) = 0$, where the value of $v_{max} > v_{ths}$ can be increased until the solution converges numerically. Eq. 47 is a regularity condition at $\lambda = 0$ which ensures that, when expressed in terms of $v_\perp = v(\lambda B/B_{max})^{1/2}$, the gyrophase averaged distribution function has the required zero derivative with respect to $v_\perp$ at $v_\perp = 0$. Finally, Eq. 48 is required so that the distribution function is continuous at the trapped-passing boundary $\lambda = 1$. The above set of boundary conditions on $K_s(v,\lambda)$ does not guarantee the physically necessary continuous derivative of the distribution function with respect to λ at the trapped-passing boundary. In order to achieve this, further analysis of a boundary layer solution near $\lambda = 1$, to be matched to the solution considered here for $\lambda < 1$, would be necessary. This would result in a modification of the boundary condition (48), to be replaced

by a condition of the form

$$K_s(v, \lambda = 1) = \nu_{*s}^{1/2} \kappa_s(v) \frac{\partial K_s(v, \lambda = 1)}{\partial \lambda}, \quad (49)$$

which introduces a finite-collisionality correction of order $\nu_{*s}^{1/2}$. This will be the subject of future work, the present paper being limited to the zeroth collisionality order results obtained with the boundary condition (48).

For the Rosenbluth potentials in Eqs. 42 and 43, we apply the following boundary conditions:

$$\Phi_s^{l,m}(v = 0) = 0 \quad (50)$$

$$\Psi_s^{l,m}(v = 0) = 0 \quad (51)$$

$$\frac{d\Phi_s^{l,m}}{dv}(v = v_{max}) = -\frac{l+1}{v_{max}} \Phi_s^{l,m}(v = v_{max}) \quad (52)$$

$$\frac{d\Psi_s^{l,m}}{dv}(v = v_{max}) = -\frac{l-1}{v_{max}} \Psi_s^{l,m}(v = v_{max}). \quad (53)$$

The conditions given by Eqs. 50 and 51 are regularity conditions at $v = 0$ for our odd values of l. Since at large v, K_s is negligible, the equation governing $\Phi_s^{l,m}$ (42) near v_{max} is essentially homogeneous. The condition given by Eq. 52 ensures that only the homogeneous solution that is regular at large v, namely $\Phi_s^{l,m} \propto v^{-l-1}$, appears in our solution there. Likewise, since $\Phi_s^{l,m}$ drives $\Psi_s^{l,m}$ in Eq. 43, the regular second Rosenbluth potential should behave like $\Psi_s^{l,m} \propto v^{-l+1}$ at large v. This condition is enforced by Eq. 53.

C. Galerkin Finite Element Method

Eq. 36 (set equal to the negative of either Eq. 37 or 38) and Eqs. 42 and 43 for all (l, m) form a closed set of coupled partial differential equations. To solve these equations, we use the Galerkin finite element method. We expand K_s in finite elements in both v and λ,

$$K_s(v, \lambda) = \sum_{i=0}^{N} \sum_{j=0}^{J} K_s^{i,j} \phi_i(v)\phi_j(\lambda). \quad (54)$$

and all of the $\Phi_s^{l,m}$ and $\Psi_s^{l,m}$ in finite elements in v,

$$\begin{pmatrix} \Phi_s^q(v) \\ \Psi_s^q(v) \end{pmatrix} = \sum_{i=0}^{N} \begin{pmatrix} \Phi_s^{i,q} \\ \Psi_s^{i,q} \end{pmatrix} \phi_i(v). \quad (55)$$

Here we have defined an index q which serves to replace the set (l, m) and runs from $q = 1, Q$ with $Q = L(M + 1)$. We use piecewise continuous linear functions for both $\phi_i(v)$ and $\phi_j(\lambda)$; these are unity on the grid points $v = v_i$ and $\lambda = \lambda_j$, respectively, and zero at all other nodes. Neither the v-grid nor the λ-grid is assumed to be uniform, allowing us to group elements in regions of particularly complex structure. All that is required is that $v_0 = 0$, $v_N = v_{max}$, $\lambda_0 = 0$, $\lambda_J = 1$, and both v_α and λ_α monotonically increase as α increases. Furthermore, we should note that a property of these linear elements is that ϕ_α only overlaps with $\phi_{\alpha+1}$ and $\phi_{\alpha-1}$.

With these elements, we apply the Galerkin method to Eqs. 36, 37, 38, 42, and 43. We introduce an inner product notation,

$$(ab)_v = \int_0^{v_{max}} ab\, dv \quad (56)$$

$$(ab)_\lambda = \int_0^1 ab\, d\lambda, \quad (57)$$

and note that any ϕ_α contained inside $(\ )_v$ is $\phi_\alpha(v)$ while any one contained inside $(\ )_\lambda$ is $\phi_\alpha(\lambda)$. Furthermore, a prime on any ϕ_α indicates a derivative with respect to the appropriate variable; thus, ϕ_α' is a piecewise constant function.

For simplicity of expressions, we multiply both $\mathcal{C}_s$ and $\mathcal{S}_s$ by v^3 before taking the weak form. Doing so, from Eq. 36,

$$\left(\phi_p v^3 \left(\phi_r \mathcal{C}_s[K_s]\right)_\lambda\right)_v = -2\left(\phi_p v^2 \nu_{Ds} \phi_i\right)_v \left(\phi_r' \eta_1 \lambda \phi_j'\right)_\lambda K_s^{i,j}$$

$$- \nu_s v_{ths}^3 \left(\phi_r \eta_2 \phi_j\right)_\lambda \left\{ \left(\phi_p' [\xi_s + \xi_{s'}] v \phi_i'\right)_v + \left(\phi_p' \left[\xi_s \frac{v^2}{v_{ths}^2} + \xi_{s'} \frac{m_s v^2}{m_{s'} v_{ths'}^2}\right] \phi_i\right)_v \right.$$

$$\left. + \frac{4\pi}{n} \left(\phi_p v^2 f_{Ms} \phi_i\right)_v \right\} K_s^{i,j}$$

$$- \frac{\nu_s v_{ths}}{n} \left(\phi_p v^2 f_{Ms} \phi_i\right)_v \left(\phi_r a^q\right)_\lambda \Phi_s^{i,q} - \frac{\nu_s}{n v_{ths}} \left(\left[\phi_p v^4 f_{Ms}\right]' \phi_i'\right)_v \left(\phi_r a^q\right)_\lambda \Psi_s^{i,q}, \quad (58)$$

where the summation over the repeated indices i, j, and q are implied. In addition, we have integrated by parts within certain inner products, noting that one or both of the finite elements are zero on the boundary of the integrals which eliminates any boundary terms. The exception to this is for the inner prod-

uct of a boundary element with itself. The equations containing such terms, however, are replaced by the boundary conditions defined in Section III B. Thus, the boundary terms are zero in all relevant cases. Applying the same operator to Eqs. 37 and 38 , we find

$$\left(\phi_p v^3 \left(\phi_r \mathcal{S}_e\right)_\lambda\right)_v = \left(\phi_r\right)_\lambda \left\{ \frac{eV_0 I}{T_e} \left(\phi_p v^3 f_{Me}\right)_v \int_0^{2\pi} \frac{\mathcal{J}}{R^2} d\theta + \frac{\nu_e v_{the}}{v_{thi}^2} \left(\phi_p v^2 \xi_i f_{Me}\right)_v \left(U_i \int_0^{2\pi} \mathcal{J} B^2 d\theta + \frac{cI}{en} \frac{dP}{d\psi} \int_0^{2\pi} \mathcal{J} d\theta\right) \right.$$
$$\left. + \frac{\nu_e m_e c I v_{the}}{e T_e} \frac{dT_e}{d\psi} \left(\phi_p v^2 \left[2\varphi_e - 10\xi_e + \frac{1}{2}\varphi_i - \frac{5v_{the}^2}{2v_{thi}^2}\xi_i\right] f_{Me}\right)_v \int_0^{2\pi} \mathcal{J} d\theta \right\} \tag{59}$$

$$\left(\phi_p v^3 \left(\phi_r \mathcal{S}_i\right)_\lambda\right)_v = - \frac{\nu_i m_i c I v_{thi}}{e T_i} \frac{dT_i}{d\psi} \left(\phi_r\right)_\lambda \left(\phi_p v^2 \left[2\varphi_i - 10\xi_i\right] f_{Mi}\right)_v \int_0^{2\pi} \mathcal{J} d\theta. \tag{60}$$

Multiplying Eqs. 42 and 43 by v^2 and then taking the weak form, the Rosenbluth potential equations become

$$\left[\left(\phi_p' v^2 \phi_i'\right)_v + l(l+1) \left(\phi_p \phi_i\right)_v\right] \Phi_s^{i,q} + \left(\phi_p v^2 \phi_i\right)_v D^{j,q} K_s^{i,j} = 0 \tag{61}$$

$$\left[\left(\phi_p' v^2 \phi_i'\right)_v + l(l+1) \left(\phi_p \phi_i\right)_v\right] \Psi_s^{i,q} + \left(\phi_p v^2 \phi_i\right)_v \Phi_s^{i,q} = 0, \tag{62}$$

where, again, integration by parts has been used and the sum over j is implied. In Eq. 61, we have inserted Eq. 54 into Eq. 44 in order to rewrite b_s^q as

$$b_s^q(v) = \sum_{i=0}^{N} \sum_{j=0}^{J} D^{j,q} K_s^{i,j} \phi_i(v) \tag{63}$$

where

$$D_{j,q} = -\frac{2(2l+1)}{1+\delta_{m,0}} \int_0^{2\pi} \cos m\theta \int_0^1 P_l(y) \frac{\phi_j(\lambda) B}{y B_{max}} d\lambda d\theta \tag{64}$$

D. Solution Method

The equation for K_s formed by setting Eq. 58 equal to the negative of Eq. 59 or 60 (depending on the species s), together with equations for the Rosenbluth potentials, Eqs. 61 and 62, can be written in the form of a single matrix equation. All homogeneous terms in those equations have a tridiagonal form in v since the velocity inner products are only nonzero for $i = p+1$, $i = p$, and $i = p-1$. Thus,

the matrix equation takes a block tridiagonal form given by

$$\mathbf{A}_s^p \cdot \mathbf{Y}_s^{p+1} - \mathbf{B}_s^p \cdot \mathbf{Y}_s^p + \mathbf{C}_s^p \cdot \mathbf{Y}_s^{p-1} = \mathbf{F}_s^p. \tag{65}$$

Here, p runs from 1 to N and the solution vectors are defined as

$$\mathbf{Y}_s^p = \begin{pmatrix} \mathbf{K}_s^p \\ \mathbf{\Phi}_s^p \\ \mathbf{\Psi}_s^p \end{pmatrix}, \tag{66}$$

where

$$\mathbf{K}_s^p = \begin{pmatrix} K_s^{p,1} \\ \vdots \\ K_s^{p,j} \\ \vdots \\ K_s^{p,J} \end{pmatrix}, \ \mathbf{\Phi}_s^p = \begin{pmatrix} \Phi_s^{p,1} \\ \vdots \\ \Phi_s^{p,q} \\ \vdots \\ \Phi_s^{p,Q} \end{pmatrix}, \ \mathbf{\Psi}_s^p = \begin{pmatrix} \Psi_s^{p,1} \\ \vdots \\ \Psi_s^{p,q} \\ \vdots \\ \Psi_s^{p,Q} \end{pmatrix}. \tag{67}$$

The matrix $\mathbf{A}_s^p$ is composed of nine submatrices and can be written in the form

$$\mathbf{A}_s^p = \begin{pmatrix} \mathbf{A}_{s1}^p & \mathbf{A}_{s2}^p & \mathbf{A}_{s3}^p \\ \mathbf{A}_{s4}^p & \mathbf{A}_{s5}^p & \mathbf{A}_{s6}^p \\ \mathbf{A}_{s7}^p & \mathbf{A}_{s8}^p & \mathbf{A}_{s9}^p \end{pmatrix}. \tag{68}$$

Likewise, $\mathbf{B}_s^p$ and $\mathbf{C}_s^p$ have similar forms. Submatrix 1 is a $J \times J$ tridiagonal matrix corresponding to the coefficients multiplying $K_s^{i,j}$ in Eq. 58. Submatrices 2 and 3 are dense $J \times Q$ matrices and correspond to the coefficients in Eq. 58 that multiply $\Phi_s^{i,q}$ and $\Psi_s^{i,q}$, respectively. Submatrix 4 is a dense $Q \times J$ matrix corresponding to the coefficient of $K_s^{i,j}$ in Eq. 61. Submatrix 5 is a diagonal $Q \times Q$ matrix corresponding to the coefficient of $\Phi_s^{i,q}$ in Eq. 61.

The $Q \times Q$ submatrix 6 and the $Q \times J$ submatrix 7 are entirely zero. Submatrices 8 and 9 are diagonal $Q \times Q$ matrices and correspond to the coefficients in Eq. 62 multiplying $\Phi_s^{i,q}$ and $\Psi_s^{i,q}$, respectively. In the elements of the submatrices defined by Eqs. 58, 61, and 62, $i = p+1$ in $\mathbf{A}_s^p$, $i = p$ for $\mathbf{B}_s^p$, and $i = p-1$ for $\mathbf{C}_s^p$. Furthermore, the elements all have opposite signs in $\mathbf{B}_s^p$ due to the sign in Eq. 65. Lastly, we note that $\mathbf{C}_s^0 = 0$ and $\mathbf{A}_s^N = 0$

The inhomogeneous term of Eq. 65, $\mathbf{F}_s^p$ is a vector composed of three subvectors:

$$\mathbf{F}_s^p = \begin{pmatrix} \mathbf{F}_{s1}^p \\ \mathbf{F}_{s2}^p \\ \mathbf{F}_{s3}^p \end{pmatrix}. \qquad (69)$$

Here, the subvector 1 has length J and corresponds to the negative of either Eq. 59 or 60, depending on the species s. Since Eqs. 61 and 62 are homogeneous, the subvectors 2 and 3 are of length Q and are both entirely zero. Finally, we note that all of these matrices may be modified on the boundary in order to enforce the boundary conditions described in Section III B.

With $\mathbf{A}_s^p$, $\mathbf{B}_s^p$, $\mathbf{C}_s^p$, and $\mathbf{F}_s^p$ all properly defined, we follow the standard block tridiagonal algorithm[21] to solve Eq. 65 for all of the $\mathbf{Y}_s^p$. This algorithm only requires inverting the matrices $\mathbf{A}_s^p$, $\mathbf{B}_s^p$, and $\mathbf{C}_s^p$, each of size $(J + 2Q) \times (J + 2Q)$, and thus scales like $O(N \times (J + 2Q)^3)$. As will be demonstrated in Section IV A, the structure in the v-direction is typically much more complex than in the λ-direction. Thus, the fact that this algorithm is linear in the number of velocity finite elements makes it particularly well-suited for solving this problem.

IV. RESULTS

A. Distribution functions

The NIES code has been used to solve for the odd contribution to the ion and electron distribution functions, K_s, on each of 64 flux surfaces in a large aspect ratio equilibrium (Figure 1a) and 128 flux surfaces in a realistic equilibrium from the National Spherical Torus Experiment[22] (NSTX) (Figure 1b). These magnetic equilibria come from the fixed-boundary, toroidal MHD equilibrium code JSOLVER[23]. We chose a one volt constant loop voltage, or $V_0 = \frac{1}{2\pi}$ volts. The density, temperature, and pressure profiles used are also shown in Figure 1, along with each equilibrium's corresponding trapped particle fraction, defined by

$$f_t = 1 - \frac{3}{4} \left\langle \frac{B^2}{B_{max}^2} \right\rangle \int_0^1 \frac{\lambda d\lambda}{\langle 1 - \lambda B/B_{max} \rangle}. \qquad (70)$$

Here, the flux surface average is defined by

$$\langle \ldots \rangle = \frac{\int_0^{2\pi} d\theta \mathcal{J} \ldots}{\int_0^{2\pi} d\theta \mathcal{J}}. \qquad (71)$$

The electron and ion temperatures are taken to be equal, though this is not required by the code. Lastly, we chose the ion mass to be that of a single proton.

Figure 2 shows a typical K_e plotted versus v (normalized to v_{the0}, the on-axis electron thermal velocity) and λ. The flux surface of this K_e is noted in Figure 1b. Slices of this distribution function are presented in Figure 3. Here we have also shown the shape of the distribution function due to each driving source term from Eq. 59. Given the chosen parameters, the ohmic drive gives by far the largest contribution to K_e. That said, at small v, the ohmic drive becomes negligibly small and the other sources dominate, mainly the pressure gradient drive. Figure 4 shows the corresponding ion solution for this flux surface.

In this study, we used a baseline case with $N = 256$ equally-spaced velocity grid points out to $v_{max} = 6v_{the0}$. In addition, we used $J = 128$ equally-spaced λ grid points, two Legendre polynomials ($L = 2$) and two Fourier modes ($M = 1$). To demonstrate convergence, we have examined the distribution function at increased resolution, maximum velocity, and mode numbers. Figure 5 shows the difference between these solutions and the baseline case for the electrons along the slices plotted in Figure 3, normalized to the peaks of the slices in the baseline case. Figures 5a and 5b demonstrate that changes in the grid spacing or size provide very little correction to the solution. As shown in Figures 5c and 5d, increasing the number of Fourier modes has a more substantial effect than increasing the number of Legendre polynomials, but these corrections are still quite small ($\lesssim 0.1\%$).
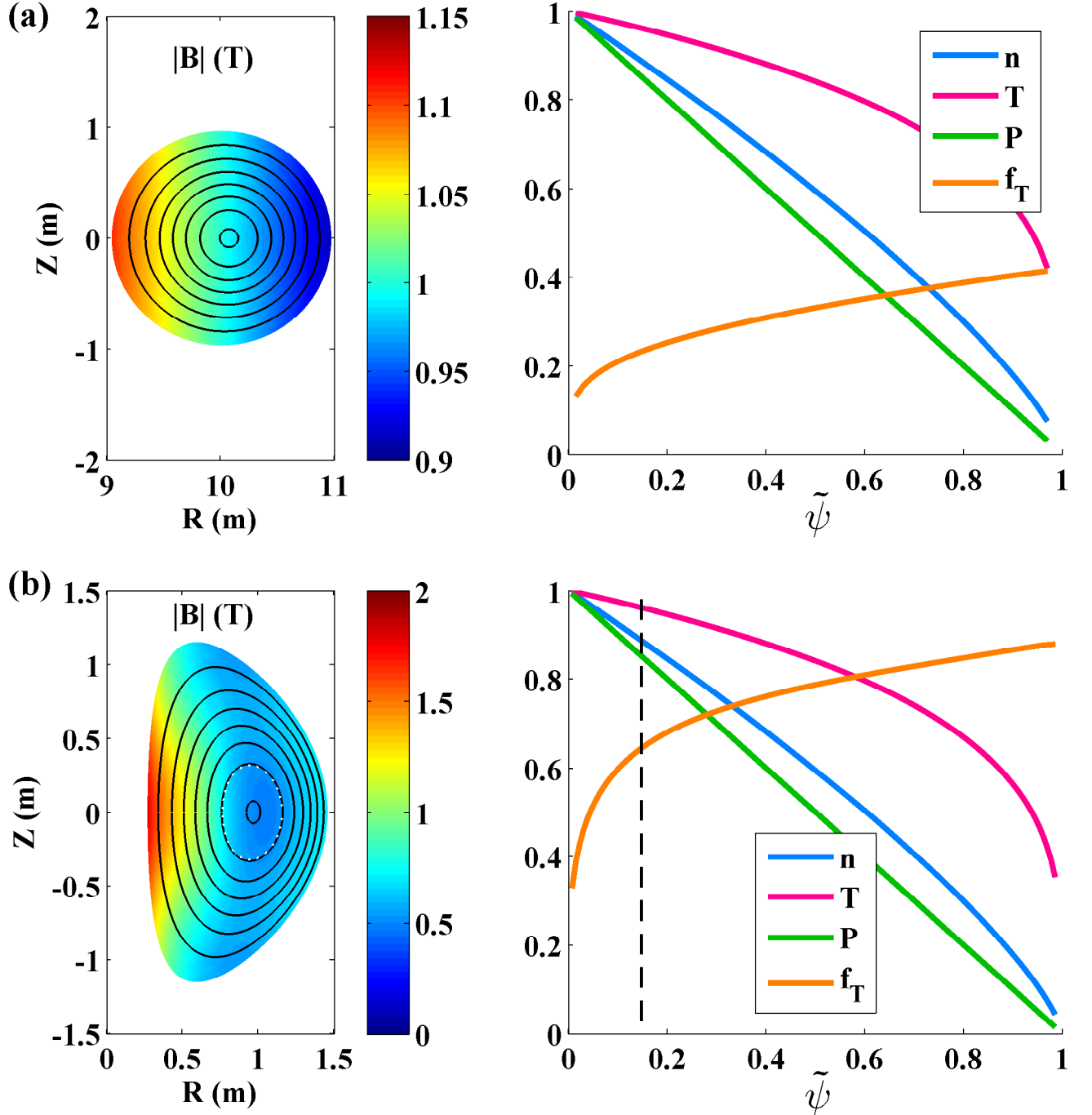
FIG. 1. (Color online). Left: The magnetic field strength in tesla in (a) a large aspect ratio JSOLVER equilibrium and (b) an NSTX JSOLVER equilibrium along with some corresponding flux surfaces. Right: For each equilibrium, the density n (normalized to $1 \times 10^{20} \mathrm{m}^{-3}$), temperature $T = T_e = T_i$ (normalized to ~ 700eV), and pressure P (normalized to $\sim 2.3 \times 10^4$Pa) used in this study. The trapped particle fraction f_T is calculated from the magnetic equilibrium on the left. In (b), the dashed flux surface on the left and the dashed line on the right show the location used for detailed study in Section IV A.
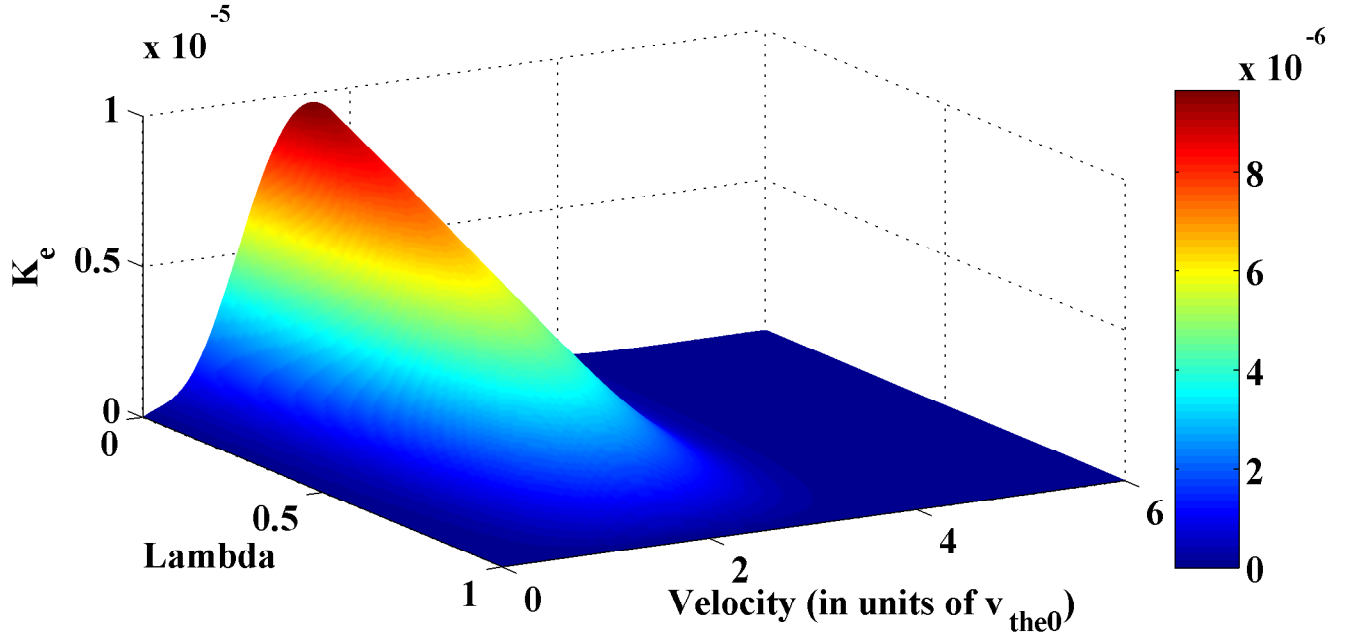
FIG. 2. (Color online). Example of the solution for K_e in an NSTX equilibrium in units of $s^3 m^{-6}$ at $\tilde{\psi} \approx 0.15$. The corresponding density, temperatures, pressure, and trapped particle fractions can be seen in Figure 1b. The relevant grid parameters are $N = 256$, $J = 128$, $L = 2$, $M = 1$, and $v_{max} = 6v_{the0}$. This N corresponds to a uniform velocity grid step size of $h_v \approx 0.023$ while this J corresponds to a uniform λ grid spacing of $h_\lambda \approx 0.0078$.
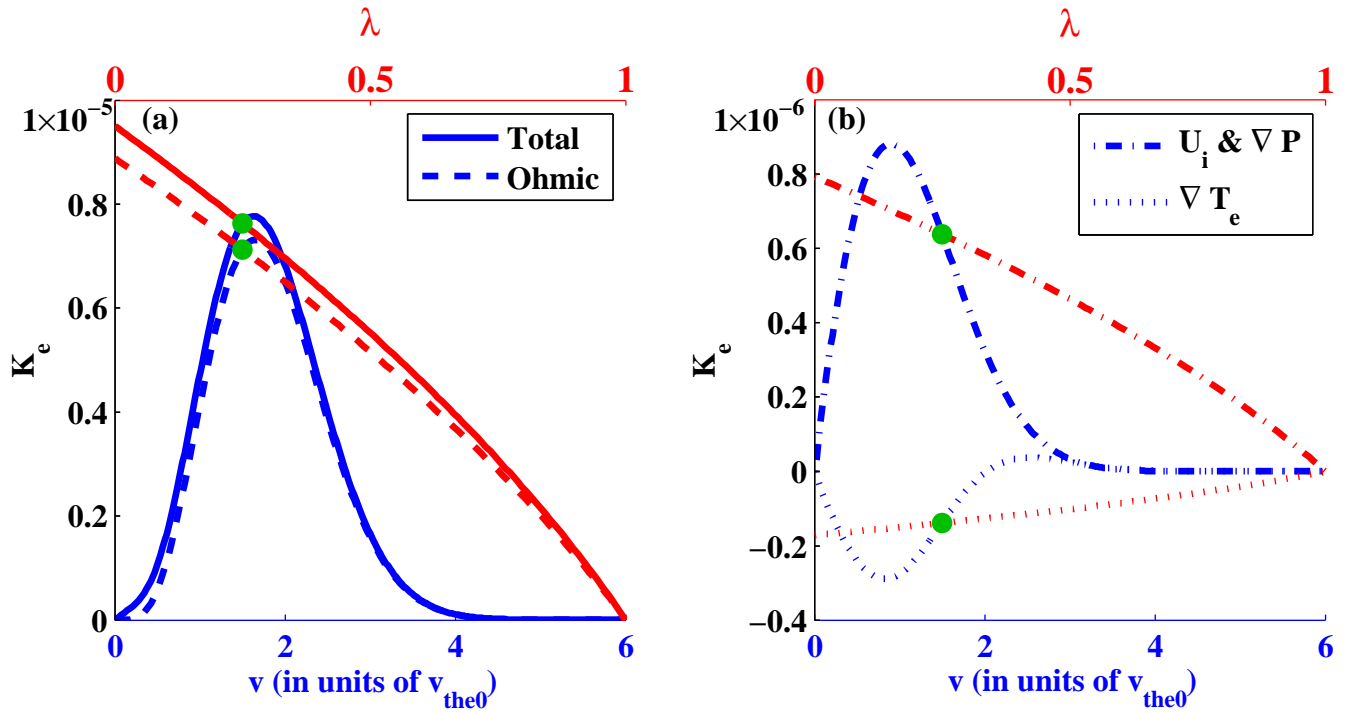
FIG. 3. (Color online). The baseline case (FIG 2) decomposed by driving source. In blue: slices along the velocity direction of the electron distribution function at $\lambda = 0.25$; use the bottom axis. In red: slices along the λ direction of the electron distribution function at $v = 1.5v_{the0}$; use the top axis. The U_i and ∇P terms are shown together as they have the same structure in velocity space (see Eq. 59). The green dots show where the corresponding velocity and λ cuts would intersect each other in a full 3D plot.
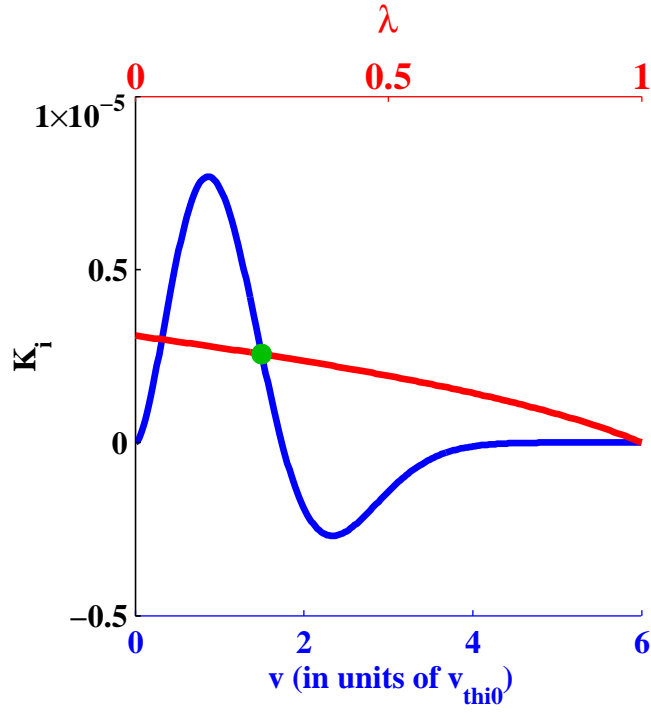
FIG. 4. (Color online). Cuts through a baseline ion distribution function using the equilibrium shown in Figure 1b and having $N = 256$, $J = 128$, $L = 2$, $M = 1$, and $v_{max} = 6v_{thi0}$. In blue: slice along the velocity direction at $\lambda = 0.25$; uses the bottom axis. In red: slice along the λ direction at $v = 1.5v_{thi0}$; uses the top axis. The green dot shows where the velocity and λ cuts would intersect each other in a full 3D plot.
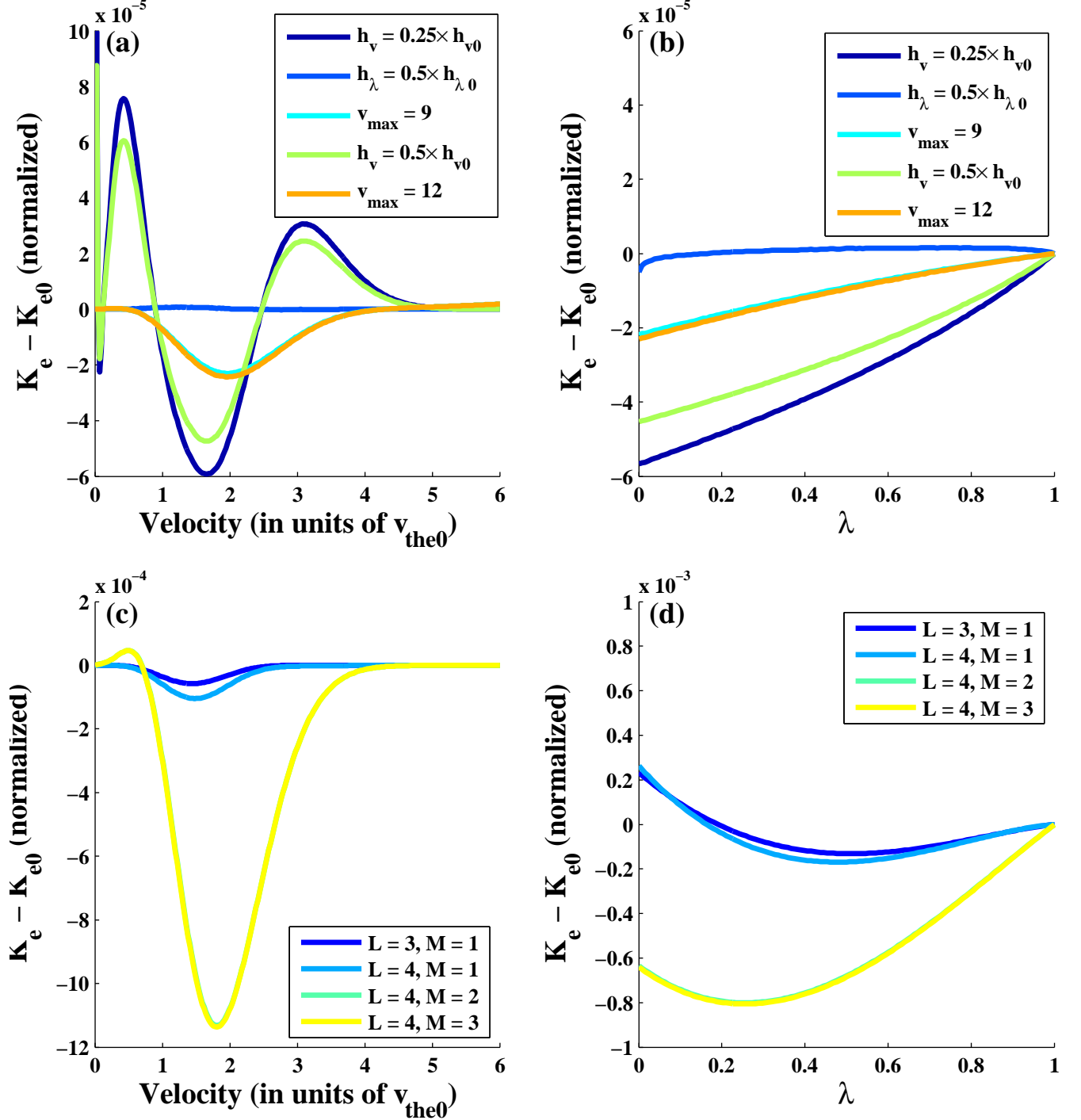
FIG. 5. (Color online). The change from the baseline case (Figure 2) for (a) a velocity cut taken along $\lambda = 0.25$ normalized to peak of this cut in the baseline case for changes in grid size, (b) a λ cut taken along $v = 1.5v_{the0}$ normalized to peak of this cut in the baseline case for changes in grid size, (c) a velocity cut taken along $\lambda = 0.25$ normalized to peak of this cut in the baseline case for changes in number of Legendre and Fourier modes, and (d) a λ cut taken along $v = 1.5v_{the0}$ normalized to peak of this cut in the baseline case for changes in number of Legendre and Fourier modes. For all curves, the parameter changed from the baseline case is noted in the legend.

B. Parallel current calculations and benchmark against Sauter's model

From Eqs. 21, 22, 26, and 27, it follows that the stream functions have the forms

$$U_e = a_0 \frac{eV_0 I \langle R^{-2} \rangle}{\nu_e m_e \langle B^2 \rangle} + a_1 \left[U_i + \frac{cI}{en \langle B^2 \rangle} \frac{dP}{d\psi} \right] + a_2 \frac{cI}{e \langle B^2 \rangle} \frac{dT_e}{d\psi} \quad (72)$$

and

$$U_i = a_i \frac{cI}{e \langle B^2 \rangle} \frac{dT_i}{d\psi}, \quad (73)$$

where a_0, a_1, a_2, and a_i are all dimensionless parameters depending only on ψ. Then, from Eq. 28, one gets

$$\langle j_\parallel B \rangle = -a_0 \frac{e^2 n}{\nu_e m_e} V_0 I \langle R^{-2} \rangle - (a_1 - 1)cI \frac{dP}{d\psi} - a_2 cnI \frac{dT_e}{d\psi} - a_i(a_1 - 1)cnI \frac{dT_i}{d\psi}. \quad (74)$$

This can be easily compared to the Sauter model[18], which provides some of the most commonly used formulas for the bootstrap current. It writes the flux surface averaged $\mathbf{j} \cdot \mathbf{B}$ as

$$\langle j_\parallel B \rangle = \sigma_{neo} \langle E_\parallel B \rangle - cI \left[\mathcal{L}_{31} \frac{dP}{d\psi} + \mathcal{L}_{32} n_e \frac{dT_e}{d\psi} + \mathcal{L}_{34} \alpha n_i \frac{dT_i}{d\psi} \right]. \quad (75)$$

The neoclassical conductivity, σ_{neo}, and the coefficients $\mathcal{L}_{31}$, $\mathcal{L}_{32}$, $\mathcal{L}_{34}$, and α were found by fitting the results for the bootstrap current from the CQLP code[13], using a linearized Fokker-Planck-Landau collision operator and the adjoint method[24] to compute only the first velocity moment of the distribution functions (as needed to determine the mean flows and current). Performing these fits over a wide variety of equilibria, they used only the trapped particle fraction, f_t, two collisionality parameters, ν_{*e} and ν_{*i}, and the ion charge, Z, as free variables. As NIES is based on a zeroth-order collisionality drift-kinetic analysis, we would expect our code to have good agreement with the Sauter model in the $\nu_{*e} = \nu_{*i} = 0$ limit with $Z = 1$. In this case, the Sauter analytic fits reduce to

$$\frac{\sigma_{neo}}{\sigma_{Sptz}} = 1 - 1.36 f_t + 0.59 f_t^2 - 0.23 f_t^3, \quad (76)$$

where $\sigma_{Sptz} \approx 1.96 \left(3\sqrt{\frac{\pi}{2}} \frac{e^2 n}{m_e \nu_e} \right)$ is the Spitzer resistivity,

$$\mathcal{L}_{31} = \mathcal{L}_{34} = 1.7 f_t - 0.95 f_t^2 + 0.15 f_t^3 + 0.1 f_t^4, \quad (77)$$

$$\mathcal{L}_{32} = -1.26(f_t - f_t^4) + 2.24(f_t^2 - f_t^4) - 1.77(f_t^3 - f_t^4), \quad (78)$$

and

$$\alpha = -\frac{1.17(1 - f_t)}{1 - 0.22 f_t - 0.19 f_t^2}. \quad (79)$$

Comparing 74 to 75, we see that

$$\sigma_{neo} = a_0 \frac{e^2 n}{\nu_e m_e} \quad (80)$$

$$\mathcal{L}_{31} = \mathcal{L}_{34} = a_1 - 1 \quad (81)$$

$$\mathcal{L}_{32} = a_2 \quad (82)$$

$$\alpha = a_i \quad (83)$$

The values for $\sigma_{neo}/\sigma_{Sptz}$, $\mathcal{L}_{31}$, $\mathcal{L}_{32}$, and $\alpha \mathcal{L}_{34}$ for both the Sauter model and the NIES code are plotted in Figure 6. The NIES values were calculated in the two equilibria described by Figure 1. The Sauter and NIES values agree universally to within a few percent. Any difference of this magnitude can likely be attributed to the Sauter model's being an analytic fit and not the exact solution for any given equilibrium. Thus, this benchmark provides verification that NIES properly solves the zeroth-order collisionality drift-kinetic equation.

The ion flow coefficient, a_i, is a common parameter of interest in its own right. We have plotted the Sauter and NIES values for this parameter in Figure 7.

V. CONCLUSION

NIES provides a new tool for calculating electron and ion distribution functions and the bootstrap current deep in the banana regime in general axisymmetric toroidal geometries and with the linearized Fokker-Planck-Landau collision operator. Efficient convergence to the values of the bootstrap current predicted by the Sauter analytic fits demonstrate that the model is correct and is being properly solved. The fact that, restricted to the leading low-collisionality (banana) order, the present NIES code obtains the full distribution functions using the Fokker-Planck-Landau collision operator, means that, in one way or another, it has some capabilities beyond those of DKES[8] or NCLASS[12]. Of the continuum codes, only the CQLP/CQL3D[13,14] codes and the most recent, Fokker-Planck version of NEO[10] are more inclusive. In any case, our approach has the unique feature of solving for the distribution functions directly in the moving reference
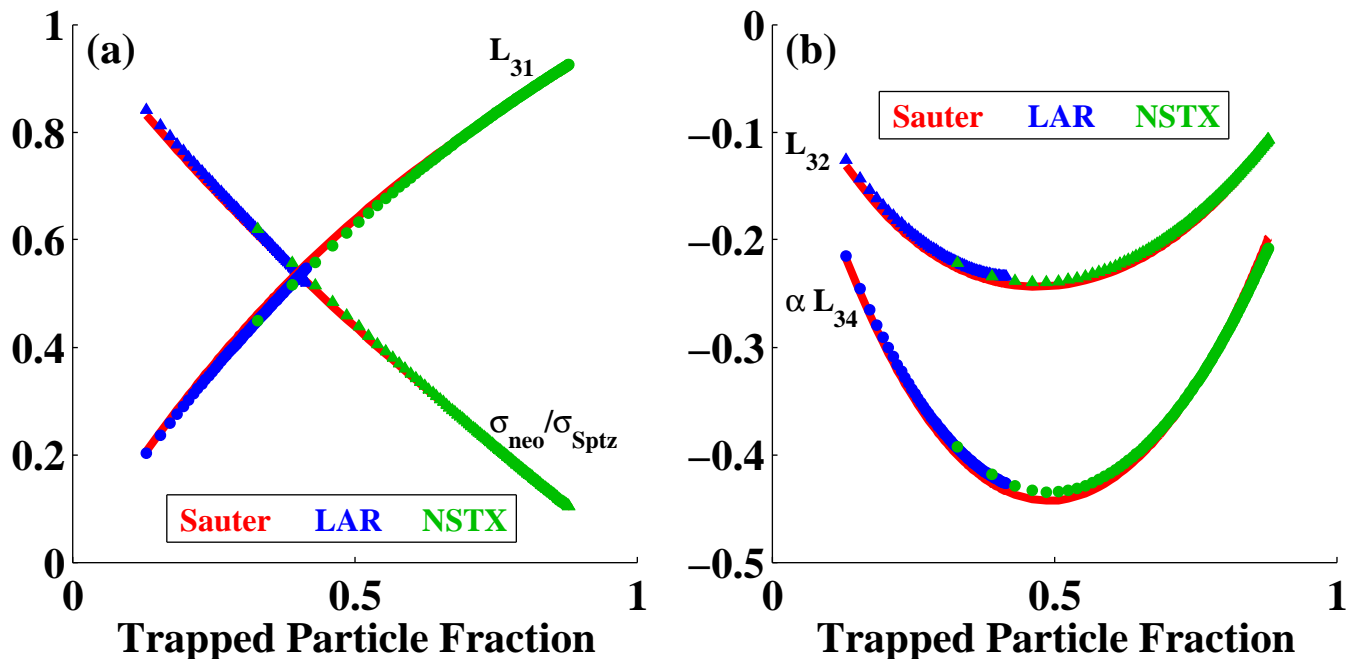
FIG. 6. (Color online). A comparison between the output of the NIES code with the Sauter analytic fits in the zeroth-order collisionality limit. The Sauter model is plotted in red. Results from NIES for a large aspect ratio (LAR) equilibrium are in blue, while the results for an NSTX equilibrium are in green. In (a), the triangles correspond to the calculated neoclassical conductivity ratio while the circles correspond to the calculated pressure gradient drive coefficient. In (b), the triangles correspond to the calculated electron temperature gradient drive coefficient, while the circles correspond to the calculated ion temperature gradient drive coefficient.

frame of each species' macroscopic flow, which simplifies the task of evaluating accurately the higher gyrotropic moments needed for the fluid closure, namely the pressure anisotropy, the parallel heat flux, and the parallel collisional friction force. The 2D NIES code provides a proof of principle that such a formulation[9,17] can be solved efficiently. We intend to continue this work in pursuit of an efficient neoclassical solver in three spatial dimensions. A first, near-term step would be to extend the code to finite but still small collisionality, allowing the distribution function to vary poloidally. In the longer term, we will work in nonaxisymmetric geometries, allowing us to solve for the bootstrap current around magnetic islands. By coupling such a code with an extended MHD solver (e.g., M3D-C1), we will be able to study the evolution of core plasma instabilities that depend on both MHD and neoclassical effects, such as the neoclassical tearing mode or sawtooth instability.

ACKNOWLEDGMENTS

[1]P.H. Rebut, R.J. Bikerton, and B.E. Keen, Nucl. Fusion 25, 1011 (1985).
[2]P.C. de Vries, M.F. Johnson, B. Alper, P. Buratti, T.C. Hender, H.R. Koslowski, V. Riccardo, and JET-EFDA Contributors, Nucl. Fusion **51**, 053018 (2011).
[3]K. Ikeda, Nucl. Fusion, **47** (2007).
[4]T.C. Hender, J.C Wesley, J. Bialek, A. Bondeson, A.H. Boozer, R.J. Buttery, A. Garofalo, T.P Goodman, R.S. Granetz, Y. Gribov, O. Gruber, M. Gryaznevich, G. Giruzzi, S. Günter, N. Hayashi, P. Helander, C.C. Hegna, D.F. Howell, D.A. Humphreys, G.T.A. Huysmans, A.W.
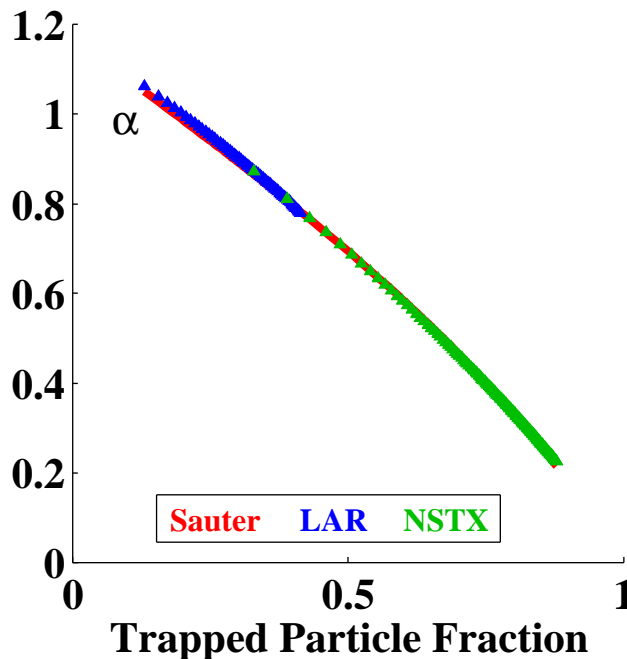
FIG. 7. (Color online). A comparison between the output of the NIES code with the Sauter analytic fits in the zeroth-order collisionality limit for the ion flow coefficient. The Sauter model is plotted in red. Results from NIES for the large aspect ratio (LAR) equilibrium are in blue, while the results for the NSTX equilibrium are in green.

Hyatt, A. Isayama, S.C. Jardin, Y. Kawano, A. Kellman, C. Kessel, H.R. Koslowski, R.J. La Haye, E. Lazzaro, Y.Q. Liu, V. Lukash, J. Manickam, S. Medvedev, V. Mertens, S.V. Mirnov, Y. Nakamura, G. Navratil, M. Okabayashi, T. Ozeki, R. Paccagnella, G. Pautasso, F. Porcelli, V.D. Pustovitov, V. Riccardo, M. Sato, O. Sauter, M.J. Schaffer, M. Shimada, P. Sonato, E.J. Strait, M. Sugihara, M. Takechi, A.D. Turnbull, E. Westerhof, D.G. Whyte, R. Yoshino, H. Zohm, and the ITPA MHD, Disruption, Magnetic Control Topical Group, Nucl. Fusion **47**, S128-S202 (2007).

[5]C.R. Sovinec, A.H. Glasser, D.C. Barnes, T.A. Gianakon, R.A. Nebel, S.E. Kruger, D.D. Schnack, S.J. Plimpton, A. Tarditi, M.S. Chu and the NIMROD Team, J. Comput. Phys., **195**, 355 (2004).

[6]S.C. Jardin, N. Ferraro, J. Breslau, and J. Chen, Computational Science & Discovery, **4** (2012).

[7]C.S. Chang, Seunghoe Ku, and H. Weitzner, Phys. Plasmas **11**, 2649 (2004).

[8]W.I. van Rij and S.P. Hirshman, Phys. Fluids B **1**, 563 (1989).

[9]J.J. Ramos, Phys. Plasmas **17**, 082502 (2010).

[10]E.A. Belli and J. Candy, Plasma Phys. Control. Fusion **54**, 015015 (2012).

[11]Code library for the ORNL Stellarator Theory and Concept Innovation Group, http://www.ornl.gov/sci/fed/Theory/stci/code_library.html, 5/7/2012.

[12]W.A. Houlberg, K.C. Shaing, S.P. Hirshman, and M.C. Zarnstorff, Phys. Plasmas **4**, 3230 (1997).

[13]O. Sauter, R.W. Harvey, and F.L. Hinton, Contrib. Plasma Phys. **34**, 2/3, pp 169-174 (1994).

[14]R.W. Harvey and M.G. McCoy, The CQL3D Code, Proc. IAEA TCM on Advances in Sim. and Modeling of Thermonuclear Plasmas, pp. 489-526, Montreal, (1992), available through USDOC/NTIS No. DE93002962; see also, http://www.compxco.com/cql3d.html, CQL3D Manual.

[15]E.A. Belli and J. Candy, Plasma Phys. Control. Fusion **50**, 095010 (2008).

[16]S.P. Hirshman and D.J. Sigmar, Nucl. Fusion **21**, 1079 (1981).

[17]J.J. Ramos, Phys. Plasmas **18**, 102506 (2011).

[18]O. Sauter, C. Angioni, and Y.R. Lin-Liu, Phys. Plasmas **6**, 2834 (1999). Erratum: **9**, 5140 (2002).

[19]M.N. Rosenbluth, R.D. Hazeltine, and F.L. Hinton, Phys. Fluids **15**, 116 (1972).

[20]F.L. Hinton and R.D. Hazeltine, Rev. Mod. Phys. **48**, 239 (1976).

[21]S. C. Jardin, *Computational Methods in Plasma Physics* (CRC Press/Taylor & Francis, Boca Raton, FL, 2010), pp 56-57.

[22]S.M. Kaye, M. Ono, Y.-K.M. Peng, D.B. Batchelor, M.D. Carter, W. Choe, R. Goldston, Y.S. Hwang, E.F. Jaeger, T. Jarboe, S. Jardin, D. Johnson, R. Kaita, C. Kessel, H. Kugel, R. Maingi, R. Majeski, J. Manickam, J. Menard, D.R. Mikkelsen, D. Orvis, B. Nelson, F. Paoletti, N. Pomphrey, G. Rewoldt, S. Sabbagh, D.J. Strickler, E. Synakowski, and J.R. Wilson, Fusion Science and Technology, **36** 16-37 (1999).

[23]J. DeLucia, S.C. Jardin. A.M.M. Todd, J. Comput. Phys. **37**, pp 183-204 (1980).

[24]T.M. Antonsen Jr. and K.R. Chu, Phys. Fluids **25**, 1295 (1982).

Information Services
Princeton Plasma Physics Laboratory
P.O. Box 451
Princeton, NJ 08543

Phone: 609-243-2245
Fax: 609-243-2751
e-mail: pppl_info@pppl.gov
Internet Address: http://www.pppl.gov